Received: 19 February 2022 | Revised: 15 September 2022 | Accepted: 26 September 2022

DOI: 10.1002/qj.4390

Quarterly Journal of the Royal Meteorological Society RMetS

RESEARCH ARTICLE

A two-fluid single-column model of turbulent shallow convection. Part III: Results and parameter sensitivity

William A. McIntyre | **Georgios A. Efstathiou** | **John Thuburn**

Department of Mathematics, College of Engineering, Mathematics and Physical Sciences, University of Exeter, Exeter, UK

Correspondence
J. Thuburn, Department of Mathematics, College of Engineering, Mathematics and Physical Sciences, University of Exeter, Exeter, EX4 4QF, UK.
Email: j.thuburn@exeter.ac.uk

Funding information
Natural Environment Research Council, Grant/Award Numbers: NE/N013123/1, NE/T003863/1; Weather and Climate Science for Service Partnership Southeast Asia, Grant/Award Number: SEA21_2.10

Abstract

Two-fluid modelling has recently emerged as a promising approach to representing cumulus convection in weather and climate models. This study applies the two-fluid model described in Part II to a shallow cumulus convection case study over land (ARM). Large-eddy simulation data are used to tune the majority of the closures that determine the properties of entrained and detrained air. The two-fluid model is generally able to reproduce the profiles of the mean and turbulent quantities over all stages of the diurnal cycle. As such, the initiation of shallow convection and the evolution of the cloud layer are well captured. The robustness of the two-fluid model is verified further using a steady-state test case (BOMEX), in which the cloud properties are also well modelled.

KEYWORDS

ARM, BOMEX, conditional filtering, multifluid modelling, NWP, shallow convection

1 | INTRODUCTION

This article is the third in a three-part series that documents progress in the development of a two-fluid single-column model and its application to simulating shallow cumulus convection. Part I (Thuburn *et al.,* 2022a) derived the equations for subfilter-scale turbulent second moments. Part II (Thuburn *et al.,* 2022b) presented a new model formulation, including new prognostic equations, closures, and numerics. This article tunes the closures from Parts I and II using large-eddy simulation (LES) data and applies the two-fluid model to two shallow cumulus convection case studies.

The modelling of atmospheric convection for regional/global weather and climate models continues to be a challenge using current approaches (Holloway *et al.,* 2014; Gross *et al.,* 2018). As the horizontal resolution of forecasting models approaches the length-scales of shallow and deep convection, the convective clouds and their associated circulations can neither be modelled by traditional parameterizations (Arakawa, 2004) nor be resolved explicitly via the dynamical core (Satoh *et al.,* 2019).

Multifluid models have recently been proposed as a potential solution to the convection modelling deadlock (Thuburn *et al.,* 2018). The method can be thought of as an extension of *traditional* mass-flux convection schemes where, instead of the convection being diagnosed regularly from grid-scale variables (e.g., Gregory and Rowntree, 1990; Neggers *et al.,* 2002; Pergaud *et al.,* 2009), convective motions are treated as a separate fluid partition

from the stable environment, with their own prognostic quantities that are computed directly by the dynamical core. As such, a multifluid representation of convection has the potential to utilize the *best of both worlds* when it comes to the grey-zone physics–dynamics coupling problem.

- The *dynamics* computes the ensemble of convective motions at any resolution in a consistent manner. Thus, a multifluid scheme incorporates some dynamical convective memory by default (Thuburn *et al.,* 2018), and allows convection to propagate to (and influence the grid-scale flow in) neighbouring columns, when used in a multicolumn configuration (Weller and McIntyre, 2019; McIntyre, 2020; Shipley, 2021). Multifluid models also have the potential to be scale-aware if coupling between the fluids is modelled appropriately to account for the filter scale (Shipley, 2021). Various studies have captured similar effects in modified mass-flux schemes—such as those of Kuell and Bott (2008), who spread the subsidence due to convection over multiple columns, and Kwon and Hong (2017), who present a scale-aware mass-flux scheme—but none of these breakthroughs has been sufficient to address all of the major biases that hinder the accuracy of the current generation of mass-flux parameterizations.
- Convection parameterizations have historically been implemented as single-column models (SCMs), as part of the model *physics*. As such, decades of research have focused on closures for convection schemes, such as entrainment and detrainment (e.g., Houghton and Cramer, 1951; Kain and Fritsch, 1990; Stirling and Stratton, 2012; De Rooy *et al.,* 2013; Willett and Whitall, 2017) or convective initiation (e.g., Betts, 1986; Fletcher and Bretherton, 2010). In a multifluid model, terms are still needed to represent entrainment and detrainment processes (modelled as relabelling of the fluid components; Thuburn *et al.,* 2019; Weller *et al.,* 2020), meaning multifluid schemes can take advantage of existing closures.

Given these features, multifluid models have the potential to converge to single-fluid solutions at high resolution ($\Delta x \ll 1\,\text{km}$), perform *at least* as well as existing parameterizations at coarse resolutions ($\Delta x \gg 10\,\text{km}$), and perform better than existing parameterizations in the intermediate grey zone.

The extended eddy diffusivity mass flux (extended-EDMF) scheme (a close cousin of the multifluid model that extends traditional EDMF schemes to include transience; Tan *et al.,* 2018) has seen substantial progress in recent years, with the formulation of new closures and successful single-column simulations of various moist convective regimes, including shallow convection (Cohen *et al.,* 2020; He *et al.,* 2020; Lopez-Gomez *et al.,* 2020). Rapid progress has also been made in developing the multifluid approach, including new numerical methods (Weller and McIntyre, 2019), new closures (Weller *et al.,* 2020), and accurate simulations of dry convection (Thuburn *et al.,* 2019; Weller *et al.,* 2020; Shipley *et al.,* 2022). The successes of both the extended-EDMF and the multifluid models have emphasized the need to account consistently for transience in the parameterization of convection, which is currently unique to these models. With the aim of advancing the multifluid model further, this article focuses on using the new multifluid higher-order-moment terms from Thuburn *et al.,* (2022a) and the new closures and numerics from Thuburn *et al.* (2022b) to simulate shallow convection over land (Atmospheric Radiation Measurement (ARM) case) and ocean (Barbados Oceanographic and Meteorological EXperiment (BOMEX) case) using a two-fluid single-column model (2FSCM).

Brown *et al.* (2002) performed a LES of the formation and evolution of shallow cumulus over the ARM Southern Great Plains site in June 1997. In their intercomparison study they used idealizations of the measured intitial profiles and forcings. Along with shallow convection case studies over the sea, such as BOMEX (Holland and Rasmusson, 1973; Nitta and Esbensen, 1974) and the Atlantic Trade wind EXperiment (Augstein *et al.,* 1973), the idealized ARM case has been used as a benchmark to test convection parameterizations in single-column models for several decades (including Golaz *et al.,* 2002; Lenderink *et al.,* 2004; Neggers *et al.,* 2004; Soares *et al.,* 2004; Rio and Hourdin, 2008; Pergaud *et al.,* 2009; Bogenschutz and Krueger, 2013; Cohen *et al.,* 2020). ARM is a discriminating test case for SCMs, involving transient growth and decay of the cloud field, ballistic behaviour of updrafts (i.e., driven by momentum rather than buoyancy at some heights), and strong "sorting" of updrafts through detrainment. The ARM case is therefore chosen as the main focus for model tuning in this article.

The two-fluid single-column model is summarized in Section 2 and the LES of the ARM case is described in Section 3. Initialization and tuning of the 2FSCM are described in Section 4, as well as comprehensive results and analysis of the 2FSCM ARM simulation. As an additional validation, the 2FSCM is tested for the BOMEX case in Section 5, which is not used for model tuning. The BOMEX case is steady-state and contains several large-scale forcing contributions that are negligible in the ARM case—the case study is therefore a useful test of the 2FSCM's robustness.

2 | TWO-FLUID SINGLE-COLUMN MODEL (2FSCM)

2.1 | Governing equations

The governing equations are adapted from the conditionally filtered compressible Euler equations (Thuburn *et al.*, 2018) for a single-column setting, where horizontal gradients are neglected. Additional equations for higher-order moment terms were derived in Thuburn *et al.*, (2022a). Each of the two fluids (with subscripts $i \in \{1, 2\}$) has prognostic equations for the mass per unit volume (m_i), entropy (η_i), specific humidity (q_i), velocity components (u_i, v_i, w_i), and turbulent kinetic energy (TKE, k_i), respectively:

$$\frac{\partial m_i}{\partial t} + \frac{\partial F_i}{\partial z} = (\mathcal{M}_{ij} - \mathcal{M}_{ji}), \tag{1}$$

$$\frac{\partial}{\partial t}(m_i\eta_i) + \frac{\partial}{\partial z}(F_i\eta_i + F_{\mathrm{SF}}^{\eta_i}) = (\mathcal{M}_{ij}\hat{\eta}_{ij} - \mathcal{M}_{ji}\hat{\eta}_{ji}) + R_i^{\eta} + S_i, \tag{2}$$

$$\frac{\partial}{\partial t}(m_i q_i) + \frac{\partial}{\partial z}\left(F_i q_i + F_{\mathrm{SF}}^{q_i}\right) = (\mathcal{M}_{ij}\hat{q}_{ij} - \mathcal{M}_{ji}\hat{q}_{ji}) + R_i^{q}, \tag{3}$$

$$\frac{\partial}{\partial t}(m_i u_i) + \frac{\partial}{\partial z}\left(F_i u_i + F_{\mathrm{SF}}^{u_i}\right) - f m_i(v_i - v_{\mathrm{g}}) = (\mathcal{M}_{ij}\hat{u}_{ij} - \mathcal{M}_{ji}\hat{u}_{ji}) + R_i^{u}, \tag{4}$$

$$\frac{\partial}{\partial t}(m_i v_i) + \frac{\partial}{\partial z}\left(F_i v_i + F_{\mathrm{SF}}^{v_i}\right) + f m_i(u_i - u_{\mathrm{g}}) = (\mathcal{M}_{ij}\hat{u}_{ij} - \mathcal{M}_{ji}\hat{u}_{ji}) + R_i^{v}, \tag{5}$$

$$\frac{\partial}{\partial t}(m_i w_i) + \frac{\partial}{\partial z}\left(F_i w_i + F_{\mathrm{SF}}^{w_i}\right) + m_i\left(\frac{1}{\rho_i}\frac{\partial p}{\partial z} + \frac{\partial \Phi}{\partial z}\right) + \mathcal{P}_i = (\mathcal{M}_{ij}\hat{w}_{ij} - \mathcal{M}_{ji}\hat{w}_{ji}) + R_i^{w}, \tag{6}$$

$$\frac{\partial}{\partial t}(m_i k_i) + \frac{\partial}{\partial z}\left(F_i k_i + \frac{1}{2}T_i^{w\mathbf{u}.\mathbf{u}}\right) = \frac{\sigma_i}{\rho_i}B_i^{\rho w}\frac{\partial p}{\partial z} + \sigma_i(w_2 - w_1)\mathcal{P}_2 - \mathbf{F}_{\mathrm{SF}}^{\mathbf{u}_i}\cdot\frac{\partial \mathbf{u}_i}{\partial z} + \tilde{\mathcal{R}}_i^{k} + R_i^{k} - \mathcal{D}_i^{k}, \tag{7}$$

$$\sum_{i=1}^{2}\sigma_i = 1, \tag{8}$$

where σ_i is the volume fraction, ρ_i is the density, p is the pressure, $\mathcal{P}$ is the pressure drag, Φ is the geopotential, u_{g} and v_{g} are the geostrophic wind components, f is the Coriolis parameter, $F_i = m_i w_i = \sigma_i \rho_i w_i$ is the mass flux, and $F_{\mathrm{SF}}^{\psi_i}$ is the subfilter flux for a fluid property ψ_i. Relabelling terms (entrainment and detrainment processes) are represented by $\mathcal{M}_{ij}$, and the properties of the relabelled components are given by $\hat{\psi}_{ij}$. Additional source/sink terms include R_i^{ψ}, which represents the transfer of properties across fluid boundaries by turbulent diffusion, and S_i, which represents a source in entropy due to the dissipation of turbulent kinetic energy. The additional terms that feature in the TKE equation are $T_i^{w\mathbf{u}.\mathbf{u}}$, which represents the subfilter turbulent flux (third-order term), $B_i^{\rho w}$, which is a buoyancy-flux term, $\tilde{\mathcal{R}}_i^{k}$, which is the total change in TKE due to the $\mathcal{M}_{ij}$ relabelling terms, and $\mathcal{D}_i^{k}$, which represents the dissipation of TKE. The equations for the subfilter terms are based on a level-2.5 multifluid Mellor–Yamada scheme (see Part I for full details; Thuburn *et al.*, 2022a) and thus neglect transience, advection, and third-order turbulent fluxes (except in the TKE equation). Full details of the chosen higher-order terms and closures are detailed in Thuburn *et al.*, (2022b), and a summary of all parameters is provided in Table 1.

2.2 | Closures for the entrainment and detrainment

Thuburn *et al.* (2022b) describe how all terms in Equations (1)–(7) are closed. However, the closures for the entrained and detrained fluid properties contain tunable parameters that should be informed by LES data.

The total entrainment/detrainment contributions are given by

$$\mathcal{M}_{ij} = \mathcal{M}_{ij}^{\mathrm{INS}} + \mathcal{M}_{ij}^{\mathrm{FRC}} + \mathcal{M}_{ij}^{\mathrm{MIX}} + \mathcal{M}_{ij}^{\mathrm{MIC}}, \tag{9}$$

where $\mathcal{M}_{ij}$ represents the relabelling rate from fluid j to fluid i. The various relabelling contributions are defined in Table 2. The different contributions correspond roughly, though not exactly, to the "*turbulent*" and "*dynamic*" entrainment/detrainment processes distinguished by De Rooy *et al.* (2013). $\mathcal{M}_{ij}^{\mathrm{INS}}$ entrains air into fluid 2 (updraft/-convective fluid) when the environment is unstable, for example, where surface heating produces buoyant air near the surface. $\mathcal{M}_{ij}^{\mathrm{FRC}}$ represents bulk detrainment from fluid 2 at the top of the boundary layer and the top of the cloud layer. The term is proportional to the vertical velocity convergence and is equivalent to the relabelling term that was successfully used in the two-fluid simulations of dry convection in Weller *et al.* (2020) and Shipley *et al.* (2022).

TABLE 1 Mathematical notation used in this document

Symbol	Formula	Description
Φ	gz	Geopotential
f		Coriolis parameter
u_g, v_g		Imposed geostrophic wind components
p		Filter-scale pressure (same in both fluids)
σ_i		Filter-scale volume fraction of fluid i
ρ_i		Filter-scale density of fluid i
m_i	$\sigma_i \rho_i$	
ρ	$\sum_i m_i$	Mean density over all fluids
η_i		Filter-scale entropy of fluid i
q_i		Filter-scale total specific humidity of fluid i
u_i, v_i, w_i		Filter-scale velocity components of fluid i
F_i	$m_i w_i$	Vertical mass flux in fluid i
$F_{\mathrm{SF}}^{\psi_i}$		Subfilter-scale vertical flux of ψ in fluid i
$\mathcal{P}_i$		Vertical drag due to subfilter-scale pressure fluctuations
$\mathcal{M}_{ij}$		Filter-scale rate per unit volume at which mass is relabelled from type j to type i
$\hat{\psi}_{ij}$		Mean value of any variable ψ in fluid that is relabelled from type j to type i
$\mathcal{F}^{\mathrm{PROC}}$		Tunable parameter that controls the mass relabelling rate for a given process
$b_{\psi,ij}^{\mathrm{PROC}}$		Tunable parameter that controls $\hat{\psi}_{ij}$ for a given process
k_i		Subfilter-scale TKE in fluid i
R_i^{ψ}		Additional effective relabelling effect on any variable ψ associated with vertical subfilter-scale fluxes and vertical variation of σ_i
D_i^{ψ}		Rate of molecular dissipation of TKE ($\psi = k$) or other second-moment quantity
S_i		Effective filter-scale entropy source in fluid i due to TKE dissipation
A_1^{MY}		Mellor–Yamada coefficient that controls the dissipation time-scale of turbulent fluxes of momentum
A_2^{MY}		Mellor–Yamada coefficient that controls the dissipation time-scale of scalar fluxes
B_1^{MY}		Mellor–Yamada coefficient that controls the dissipation time-scale for the velocity variances
B_2^{MY}		Mellor–Yamada coefficient that controls the dissipation time-scale for other scalar variances

Convergence-based entrainment/detrainment closures have also been used in mass-flux convection schemes (Houghton and Cramer, 1951; Kuell and Bott, 2008; De Rooy *et al.*, 2013). Here, this term is only used for detrainment, as an entrainment contribution would cause double-counting at the surface when combined with the instability entrainment term. Finally, $\mathcal{M}_{ij}^{\mathrm{MIX}}$ and $\mathcal{M}_{ij}^{\mathrm{MIC}}$ represent turbulent mixing in the boundary layer and cloud layer respectively, and are approximately proportional to the square root of the fluid 2 TKE (the limit shown in Table 2) except when the updraft fraction is very small.

The properties of the relabelled fluid components for some variable ψ are given by

$$\mathcal{M}_{ij}\hat{\psi}_{ij} = \mathcal{M}_{ij}^{\mathrm{INS}}\hat{\psi}_{ij}^{\mathrm{INS}} + \mathcal{M}_{ij}^{\mathrm{FRC}}\hat{\psi}_{ij}^{\mathrm{FRC}} + \mathcal{M}_{ij}^{\mathrm{MIX}}\hat{\psi}_{ij}^{\mathrm{MIX}} + \mathcal{M}_{ij}^{\mathrm{MIC}}\hat{\psi}_{ij}^{\mathrm{MIC}}, \tag{10}$$

where the relabelled fluid property for a given process (PROC) is a linear combination of the fluid i and j properties,

$$\hat{\psi}_{ij}^{\mathrm{PROC}} = \left(1 - b_{\psi,ij}^{\mathrm{PROC}}\right)\psi_i + b_{\psi,ij}^{\mathrm{PROC}}\psi_j, \tag{11}$$

TABLE 2 The four methods for entraining and detraining air from the convective fluid

Symbol	Formulation	Process	Direction
$\mathcal{M}_{ij}^{\mathrm{INS}}$	$= \mathcal{F}^{\mathrm{INS}} m_1 \sqrt{-\min\left(0, N_1^2\right)}$	Instability entrainment	$1 \rightarrow 2$
$\mathcal{M}_{ij}^{\mathrm{FRC}}$	$= \mathcal{F}^{\mathrm{FRC}} m_2 \ \max\left(0, -dw_2/dz\right)$	Forced detrainment	$2 \rightarrow 1$
$\mathcal{M}_{ij}^{\mathrm{MIX}}$	$\approx \mathcal{F}^{\mathrm{MIX}} m_i \sigma_j (1 - W^{\mathrm{CLD}}) \sqrt{k_2} / L_i^{\mathrm{PLM}}$	Turbulent mixing (dry)	Both
$\mathcal{M}_{ij}^{\mathrm{MIC}}$	$\approx \mathcal{F}^{\mathrm{MIC}} m_i \sigma_j W^{\mathrm{CLD}} \sqrt{k_2} / L_i^{\mathrm{PLM}}$	Turbulent mixing (cloud)	Both

Note: Note that these processes represent the contributions to the $\mathcal{M}_{ij}$ term only and not R_i. The formulation of the turbulent mixing terms $\left(\mathcal{M}_{ij}^{\mathrm{MIX}} \text{ and } \mathcal{M}_{ij}^{\mathrm{MIC}}\right)$ is given in the limit where the updraft volume fraction is not small ($\sigma_2 \gg 10^{-3}$); the full formulation is given in Part II Thuburn *et al.* (2022b). $\mathcal{F}^{\mathrm{INS}} = 0.2$, $\mathcal{F}^{\mathrm{FRC}} = 1$, and $\mathcal{F}^{\mathrm{MIX}} = \mathcal{F}^{\mathrm{MIC}} = 0.4$ are tunable parameters that determine the magnitude of the relabelling term. $N_i \approx \sqrt{\frac{g}{\theta_i} \frac{\partial \theta_i}{\partial z}}$ is the Brunt–Väisälä frequency for fluid i. L_i^{PLM} is the plume length-scale, which is calculated from the height, TKE, and Brunt–Väisälä frequency (Thuburn *et al.*, 2022b). W^{CLD} is a weighting that transitions smoothly between cloudy ($W^{\mathrm{CLD}} = 1$) and noncloudy regions ($W^{\mathrm{CLD}} = 0$).

and $b_{\psi,ij}^{\mathrm{PROC}}$ is a tunable parameter. The values for $b_{\psi,ij}^{\mathrm{PROC}}$ will be diagnosed in Section 3.2.

2.3 | Discretization summary

The full description of the numerical methods is given in Part II (Thuburn *et al.*, 2022b). The two-fluid model uses a semi-implicit Eulerian discretization. The time discretization is off-centred Crank–Nicolson using an off-centring coefficient of 0.55 and a time step of 30 s. This time step is considerably longer than the maximum time step achieved in the semi-Lagrangian model version of Thuburn *et al.* (2019), but further development is needed to enable the approach to work with the even longer time steps currently used with operational mass-flux schemes. The spatial discretization uses a Charney–Phillips grid where p, ρ, u, v, and the second moments are stored at cell centres, and w, η, and q are stored at the cell faces. The system of equations is solved using a quasi-Newton method, where separate linear systems are solved for the first-order moments (with the exception of the horizontal velocity components) and the second-order moments. Splitting the solver up in this way reduces the computational cost whilst retaining the most important couplings and thus allowing the solver to converge.

3 | LARGE-EDDY SIMULATION OF THE ARM CASE

3.1 | LES setup and validation

As a benchmark solution for the 2FSCM, the ARM case has been simulated using the Met Office/NERC[1] Cloud Model (MONC). The idealized profiles of potential temperature and moisture from Brown *et al.* (2002) are used as initial conditions, with the atmosphere in hydrostatic balance. The vertical velocity components are initially zero, with the horizontal components equal to the geostrophic forcings. The prescribed forcing for the horizontal winds, surface sensible heat flux, and surface latent heat flux is also used from Brown *et al.* (2002). The LES is run on a uniform Cartesian grid, with a horizontal resolution of 50 m over a domain of $19.2 \times 19.2\,\mathrm{km}^2$ and vertical resolution of 20 m up to a height of 4.4 km. The Smagorinsky scheme is used to represent turbulent scales that are smaller than the grid scale (Smagorinsky, 1963). The model was run for 14 hr with a variable time step that keeps the Courant number at a stable value.

As the results of the LES simulation are to be compared with the two-fluid model, the 3D fields need to be partitioned into updraft and environment fluids. The Couvreux *et al.*, (2010); Efstathiou *et al.*, (2020) definition for coherent structures, which uses radioactive tracers, will be used to define the updraft/convective fluid:

$$I_2(x,y,z) = \begin{cases} 1, & \text{if } \chi_{\mathrm{r}}'(x,y,z) > \max[s_{\chi_{\mathrm{r}}}(z), s_{\min}(z)] \\ & \quad \text{and } w(x,y,z) > 0, \\ 0, & \text{otherwise,} \end{cases} \tag{12}$$

where $I_2(x,y,z)$ is a binary indicator for whether fluid 2 (updraft) exists at that location, χ_{r}' is defined as $\chi_{\mathrm{r}}'(x,y,z) = \chi_{\mathrm{r}}(x,y,z) - \overline{\chi}_{\mathrm{r}}(z)$, $\chi_{\mathrm{r}}(x,y,z)$ is the radioactive tracer mixing ratio, $\overline{\chi}_{\mathrm{r}}(z)$ is the horizontal average of χ_{r} at height z, $s_{\chi_{\mathrm{r}}}(z)$ is the standard deviation of χ_{r} at height z, $s_{\min}(z) = 1/z \int_0^z s_{\chi_{\mathrm{r}}}(z')\, dz'$, and $w(x,y,z)$ is the vertical velocity. Results from Efstathiou *et al.* (2020) motivate the use of this fluid definition, because the resolved contributions to the vertical scalar fluxes are maximized (meaning less work has to be done by subfilter-scale parameterizations). In the LES, the radioactive tracer, χ_{r}, is uniformly emitted from the surface at a constant rate and decays with

[1]Natural Environment Research Council

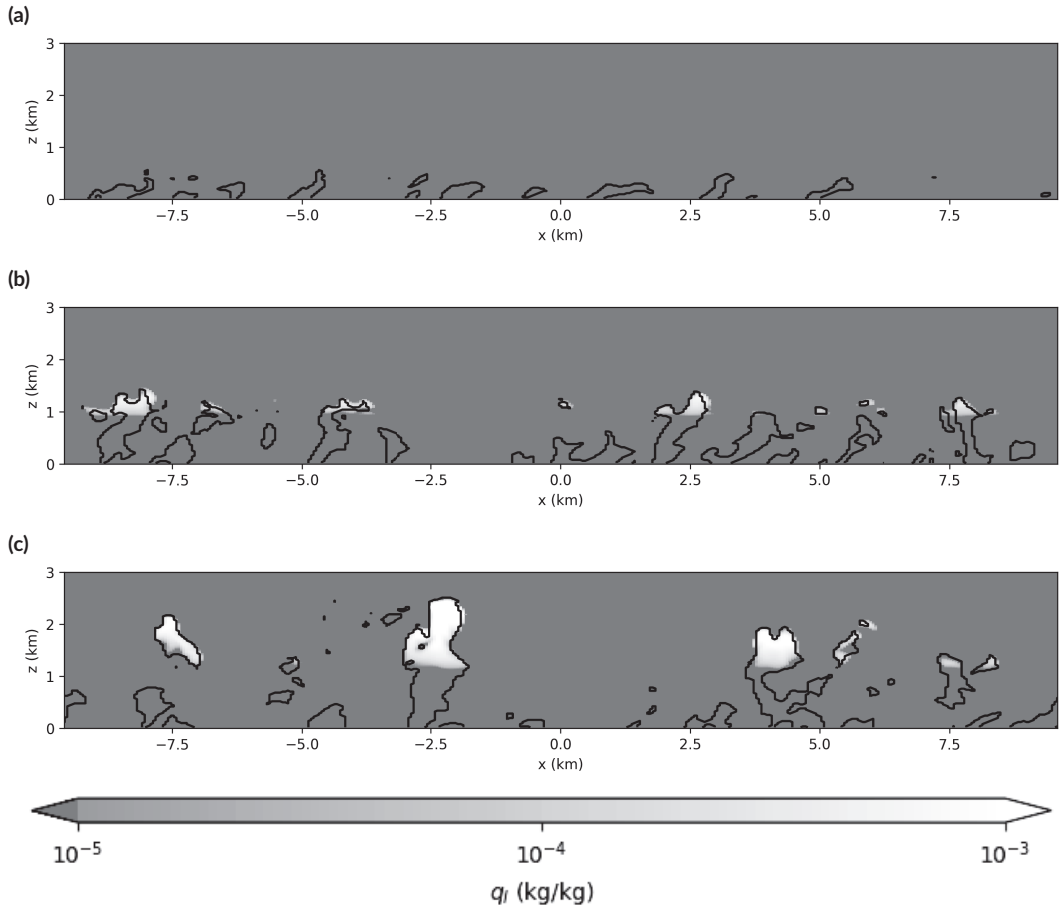

FIGURE 1 Cross-sections of the plumes (defined by Equation 12) at 3, 7, and 11 hr into the LES ARM case. The black contour defines the edges of the plumes and clouds are shown in white/light grey. (a) ARM dry phase ($t = 3$ hr); (b) ARM growth phase ($t = 7$ hr); (c) ARM mature phase ($t = 11$ hr)

a time-scale of 15 min, which is a suitable choice for the lifetime of shallow cumulus clouds. By horizontally averaging scalar quantities over regions where $I_1 = 1 - I_2 = 1$ or $I_2 = 1$, the properties of the environment and updraft can be diagnosed. The regions in which fluid 2 is defined are showcased in Figure 1 (black contours) during the growth of the moist convective boundary layer (top), the growth of the shallow cumulus layer (middle), and the quasisteady state of the shallow cumulus clouds (bottom).

Figure 2 a shows the evolution of the cloud fraction (not to be confused with the fluid 2 volume fraction) for the ARM case. Shallow cumulus clouds begin to form approximately 3.75 hr into the simulation at a height of 850 m. The clouds continue to grow and develop until a quasisteady state is reached shortly after the 8-hr mark. The cloud base (∼1.2 km) and cloud top (∼3.0 km) are then maintained for 5 hr before the cloud-base fluxes drop below the threshold to sustain convection. The cloud development as well as the vertical profiles of the grid-scale variables and fluxes (solid lines in Figures 5 and 7 later) are consistent with the ensemble of LES model results presented in Brown *et al.* (2002). Note that there is substantial variability in the cloud fraction contours, due to individual clouds that skew the horizontally averaged properties—the 2FSCM cloud fraction (calculated from the moisture and entropy covariances; Thuburn *et al.*, 2022b) is expected to be far smoother, as the cloud ensemble is modelled instead.

3.2 | Diagnosing entrainment and detrainment coefficients

An important aspect in configuring the two-fluid model is choosing suitable b coefficients for Equation (11). These coefficients determine the properties of the air entrained and detrained from a convective plume. The dimensionless b coefficient is therefore approximating the parts of the velocity, temperature, and moisture distributions that are involved in the relabelling process—much like the adaptive detrainment method by Derbyshire *et al.* (2011).

By re-arranging Equation (11), the relabelling coefficient for a specific entrainment/detrainment process is

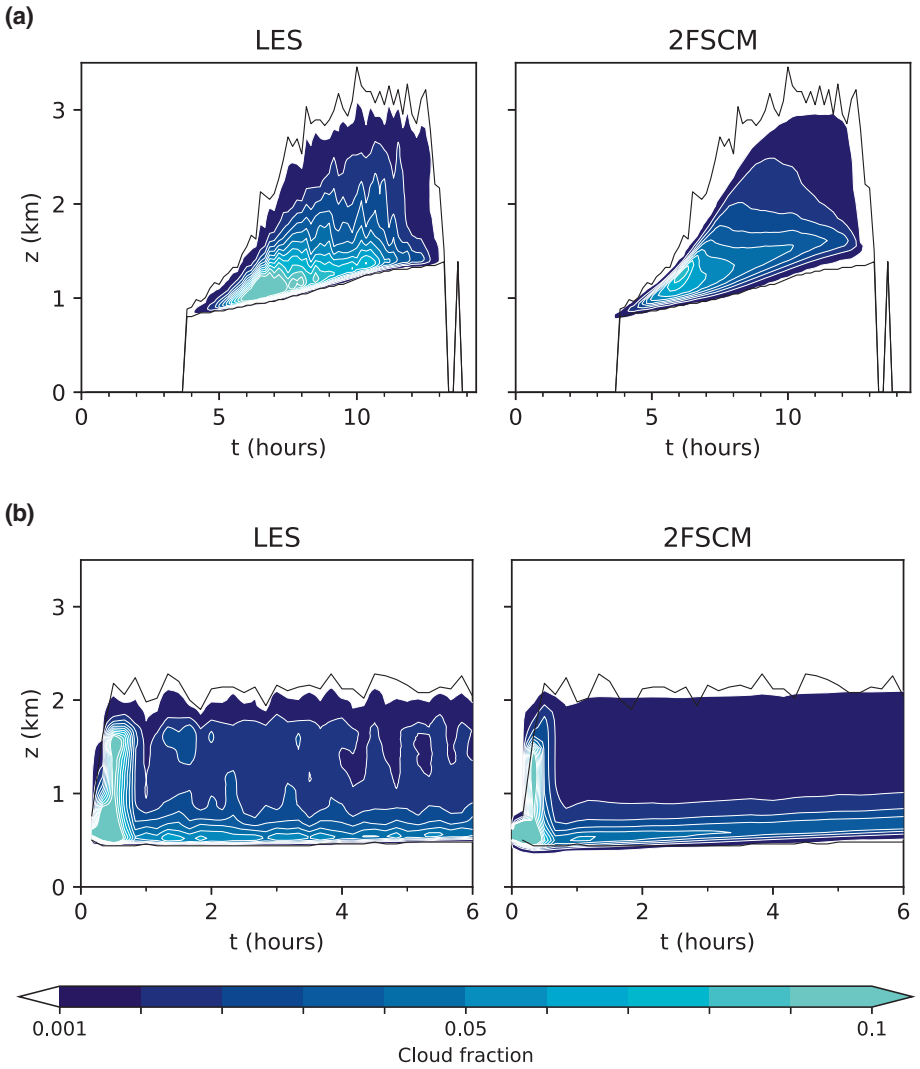

FIGURE 2 The cloud fraction for the ARM case (top) and BOMEX case (bottom) using the MONC LES model (left) and the 2FSCM (right). The white contours are in increments of 0.01, with the exception of the first filled contour which starts at a cloud fraction of 0.001. The black lines represent the minimum and maximum extent of the liquid water in the LES (cloud base and cloud top). The cloud spike after 13.5 hr in the LES ARM case is due to a single cell which is saturated at that time. (a) ARM case; (b) BOMEX case [Colour figure can be viewed at wileyonlinelibrary.com]

given by

$$b^{\mathrm{PROC}}_{\psi,ij} = \frac{\hat{\psi}^{\mathrm{PROC}}_{ij} - \psi_i}{\psi_j - \psi_i}. \tag{13}$$

The LES data can be used to estimate $b^{\mathrm{PROC}}_{\psi,ij}$ in regions where entrainment or detrainment are occurring, assuming that $\hat{\psi}^{\mathrm{PROC}}_{ij}$ can be diagnosed. Two separate methods are used to estimate $\hat{\psi}^{\mathrm{PROC}}_{ij}$.

- **Particle trajectory method**: The particle trajectory calculations use the Clark et al. (2022) method, which relies on the allocation of a set of tracer fields, advected by the Eulerian flow field, to act as *Lagrangian labels* (see also Gheusi and Stein, 2002). These labels should not be confused with the indicators produced by the radioactive tracer. Contrary to conventional trajectory calculations, where particle position is advanced forwards or backwards in time based on the simulated wind field, here the MONC advection scheme is used to transport the Lagrangian label tracers online. The tracers are output at regular intervals (here every 60 s) and can then be used for the efficient offline calculation of large numbers of backward or forward trajectories.

  Trajectories are generated for every second grid point and back trajectories are then used to simulate the movement of the Lagrangian particles. Following Yeo and Romps (2013), the horizontally averaged properties (velocity, potential temperature, moisture, etc.) of all particles that have entered or left a plume (where $I_2 = 1$) are recorded. These horizontally averaged profiles are assumed to be the entrained or detrained properties ($\hat{\psi}^{\mathrm{PROC}}_{ij}$). Local entrainment/detrainment rates are estimated by the number of particles that switch between fluid 1 and 2 and vice versa at each trajectory time step and are then horizontally averaged over bins in the vertical. It should be noted that the particles can be recirculated into cloudy thermals, especially around the cloud shell, leading to fast entrainment/detrainment events

that can affect the properties of the relabelled particles (see also Dawe and Austin, 2011).

- **Plume-edge method**: The grid cells adjacent to any plume boundary are horizontally averaged over the entire domain to give $\hat{\psi}_{ij}^{\mathrm{PROC}}$. This method assumes that any relabelling process will entrain or detrain the fluid properties that are present at the plume edge. This method does not distinguish between regions that are entraining and regions that are detraining, instead acting as an average over all relabelling processes that are present in a given layer.

Given that there are three different entrainment/detrainment mechanisms (Table 2), the relabelled property data must be partitioned further into regions where each entrainment/detrainment regime is most likely to be dominant. Figure 3 shows these idealized relabelling regions, where the following assumptions have been made.

- The top of the boundary layer, z_{BL}, is defined as the height at which the minimum in the resolved buoyancy-flux profile is attained. The assumed relabelling regions are defined relative to the cloud-top height, z_{CT}, and $z_{\mathrm{BC}} = \max\,(z_{\mathrm{BL}}, z_{\mathrm{CB}})$, where z_{CB} is the cloud-base height.
- The instability entrainment $\left(\mathcal{M}_{ij}^{\mathrm{INS}}\right)$ is most influential for $z < z_{\mathrm{CB}}$.
- The forced detrainment $\left(\mathcal{M}_{ij}^{\mathrm{FRC}}\right)$ is the dominant process at the top of the boundary layer ($0.75z_{\mathrm{CB}} < z < 1.1z_{\mathrm{CB}}$) and at the top of the cloud layer ($z_{\mathrm{CB}} + 0.75(z_{\mathrm{CT}} - z_{\mathrm{CB}}) < z < 1.1z_{\mathrm{CT}}$).
- Turbulent mixing $\left(\mathcal{M}_{ij}^{\mathrm{MIX}}$ and $\mathcal{M}_{ij}^{\mathrm{MIC}}\right)$ is the main entrainment/detrainment mechanism in the remaining regions below the cloud top.

Note that these are diagnostic limits only and do not restrict the entrainment/detrainment terms in the 2FSCM. Using the defined regions in which the relabelling schemes operate, the diagnosed relabelling coefficients for the vertical velocity, potential temperature, and moisture are shown in Figure 4. Each relabelling coefficient $\left(b_{\psi,ij}^{\mathrm{PROC}}\right)$ has a diagnosed distribution from the Lagrangian particle diagnostic (top) and the plume edge diagnostic (bottom). These distributions do not change meaningfully throughout the different phases of the simulation. The two methods for diagnosing $\psi_{ij}^{\mathrm{PROC}}$ produce some differences in the diagnosed b coefficients because the plume-edge method does not discriminate between entrainment and detrainment processes, whereas the particle method does. These diagnosed distributions can be used to select the relabelling coefficients for each relabelling process in Table 2 (see Section 4.2).

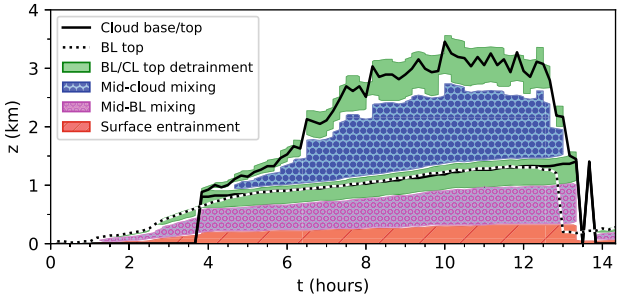

FIGURE 3 The regions in which the entrainment and detrainment processes from Table 2 are expected to be most influential. Note that the breaks or gaps in the BL/CL detrainment regions are merely an artefact of the contouring algorithm, due to sharp changes in the top of the boundary and cloud layers. Sampling entrained/detrained fluid properties in these regions can help diagnose the closure for the $b_{\psi,ij}^{\mathrm{PROC}}$ coefficients from Equation (13) (see Figure 4). Entrainment and detrainment distributions, as calculated by the 2FSCM, are presented in Figure 5 [Colour figure can be viewed at wileyonlinelibrary.com]

It is clear that these results support the idea of using different coefficients for different entrainment/detrainment processes (whereas Thuburn *et al.*, 2019, used a single coefficient for each variable at all altitudes). It is also apparent that entraining or detraining the mean properties of a fluid, achieved using $b_{\psi,ij}^{\mathrm{PROC}} = 1$, is not consistent with the majority of the diagnosed coefficients in Figure 4—mean properties were used for potential temperature in Thuburn *et al.* (2019) and for buoyancy in Weller *et al.* (2020). Instead, the diagnostics suggest that a b coefficient between 0 and 1 should be used in most cases, which is consistent with the idea that the properties at the plume edges fall in between the mean properties of the plume and the environment, and the idea that the "weakest" properties of the plume are detrained first, leaving the plume core behind (see the forced detrainment coefficient for vertical velocity, $b_{w,12}^{\mathrm{FRC}}$, for example).

4 | TWO-FLUID SCM SIMULATION OF THE ARM CASE

4.1 | Initialization and forcing

The 2FSCM is initialized with the same mean fields and forcings as the LES. The volume fractions for each fluid are set to

$$\sigma_1 = 1 - \sigma_{\min}, \tag{14}$$

$$\sigma_2 = \sigma_{\min}, \tag{15}$$

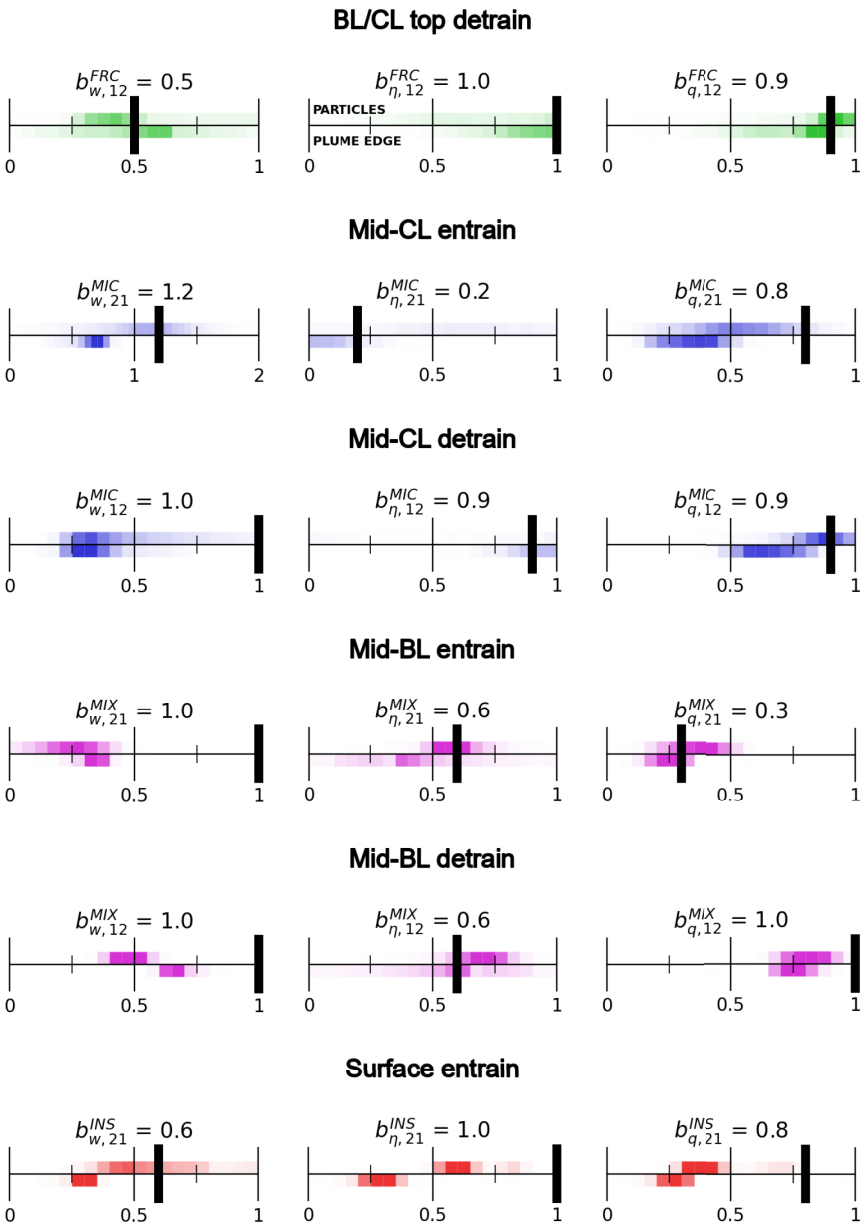

FIGURE 4 The relabelling coefficients diagnosed from the LES data, where darker shades represent higher frequencies in the binned data. For each relabelling coefficient, the top row of LES data represents the diagnosed values from the Lagrangian particle data, whereas the bottom row uses data from the edge of the plumes. Also shown are the settings used by the 2FSCM, which are represented by the vertical black markers [Colour figure can be viewed at wileyonlinelibrary.com]

where $\sigma_{\min} = 10^{-3}$ is the minimum allowed volume fraction. The potential temperature, moisture, and horizontal velocity fields (for both fluids) are set to the same initial profiles as the LES (specified in Brown *et al.,* 2002). The density and pressure are calculated so that the system is initially in hydrostatic balance. All other profiles are initialized as zero, with the exception of the TKE, which is set to the minimum allowed value of 10^{-4} m^2·s^{-2}. As with the LES, the sensible and latent surface heat fluxes are prescribed according to Brown *et al.* (2002), where the peak fluxes occur 7.5 hr into the simulation. As described in Thuburn *et al.* (2022b), the energy from the surface fluxes enters both fluids proportional to their volume fractions when the surface fluxes are negative. When the surface fluxes are positive, fluid 2 receives disproportionately more of the surface fluxes in order to distinguish fluid 2 as the convective fluid.

4.2 | Tunable parameters

The $b^{\mathrm{PROC}}_{\phi,ij}$ coefficients that determine the entrained/detrained fluid properties have been chosen with the help of the diagnosed values from the LES (see black markers in Figure 4). However, these coefficients control complicated feedbacks that can be difficult to account for, and some manual adjustments to the parameters were needed to obtain a satisfactory representation of the ARM case. As

such, four parameters $\left(b^{\mathrm{MIX}}_{w,12}, b^{\mathrm{MIX}}_{w,21}, b^{\mathrm{INS}}_{\eta,21}, b^{\mathrm{INS}}_{q,21}\right)$ have settings outside the range of the LES-diagnosed values. The vertical velocity coefficients in the boundary layer $\left(b^{\mathrm{MIX}}_{w,12}\right.$ and $\left.b^{\mathrm{MIX}}_{w,21}\right)$ are used to tune the difference in fluid vertical velocities. However, using values less than one leads to unrealistically high velocities in the boundary layer. This may hint that additional fluid pressure terms (He *et al.,* 2020; Weller *et al.,* 2020) or stronger drag terms are needed. $b^{\mathrm{INS}}_{\eta,21}$ is used to set the fluid 2 buoyancy at the surface, and $b^{\mathrm{INS}}_{q,21}$ determines the difference in moisture at the surface. Both the buoyancy and moisture differences at the surface are correct using the given coefficients.

Other tunable parameters were tuned via a gradient-descent algorithm, which was configured to minimize the root-mean-square error of the cloud fraction, the fluid 2 volume fraction, and the fluid 2 TKE (which is especially important given that multiple processes are coupled to the fluid 2 TKE). The tuned parameters include those controlling the magnitude of entrainment/detrainment for the various processes ($\mathcal{F}^{\mathrm{PROC}}$ from Table 2) as well as the coefficients that control the time-scales of subfilter fluxes and dissipation rates: A^{MY}_1, A^{MY}_2, B^{MY}_1, B^{MY}_2, which correspond to the coefficients A_1, A_2, B_1 and B_2 from the well known Mellor and Yamada (1982) turbulence closure hierarchy—see Thuburn *et al.* (2022b) for more details.

The final values of the tunable parameters are shown in Figure 4 (see also section 4.4). Results of the 2FSCM using these parameters are presented in Section 4.3, and the model sensitivity to the parameters is discussed in Section 4.4.

4.3 | Results

Figure 2 a shows the cloud fraction for the 2FSCM. The initiation of the cloud occurs at the correct time of ∼3.75 hr and the cloud base rises at a realistic rate relative to the LES for the subsequent 9 hr. The clouds grow realistically during the cloud development stage (∼4–8 hr) before maintaining the correct cloud-top height (0.1% contour) until 12 hr. The clouds dissipate half an hour earlier than the LES because the SCM boundary layer loses too much moisture due to strong vertical entrainment fluxes at the top of the boundary layer—this boundary-layer moisture deficiency can be seen in Figure 5c. The cloud fraction is approximately 25% too small in the lower cloud layer due to an excess in fluid 2 moisture variance at that height.

The vertical profiles of the mass-flux-related properties of each fluid are presented in Figure 5. LES diagnostics are shown via the solid lines and the 2FSCM results via the dashed lines. LES vertical profiles are diagnosed from the MONC simulation, with the exception of the total entrainment/detrainment, which is diagnosed from the particle method (averaged over a turnover time of ±10 min). Throughout all three phases of the ARM simulation, the volume fraction of fluid 2 maintains the correct shape, with the exception of the top of the cloud layer during the latter stages of the simulation. This can, in part, be mitigated using a larger value of A^{MY}_2, which increases the diffusion of the vertical velocity and thus reduces the detrainment due to convergence of fluid 2. The evolution of the updraft vertical velocity and the mass flux closely resemble the LES results, with the most significant exception being the local minimum in w_2 in the lower cloud layer. Entrainment and detrainment profiles are consistent in shape and magnitude relative to the LES in the boundary layer, but are too low in the cloud layer, another potential contributing factor to the reduced volume fraction in the cloud layer.

Figure 6 shows the vertical profiles for various other scalar quantities. The potential temperature closely resembles the LES throughout all phases of the simulation, but is slightly too dry in the boundary layer. The water-vapour profile is also too dry in the boundary layer. This difference is likely due to a collective effect of the chosen relabelling coefficients $\left(b^{\mathrm{PROC}}_{\psi,ij}\right)$, as well as too much dry air diffusing into the boundary layer. This is also thought to be why the boundary-layer height (and cloud base) rises too far after the 10th hour in Figure 2. The same issue appears in other convection schemes (see Neggers *et al.,* 2004; Lenderink *et al.,* 2004, for example). Future research will focus on modelling the fallback of overshooting thermals in order to return more moist and cool air into the boundary layer. This process involves countergradient subfilter-scale fluxes that cannot be represented by the downgradient eddy-diffusion parameterizations used in this study.

The mean liquid water in fluid 2 is too large in the later stages of the simulation, although the mass-weighted liquid is approximately correct given the smaller volume fraction in the upper cloud layer relative to the LES. This overestimation of liquid water is likely due to insufficient entrainment in the cloud layer, as fluid 2 is not mixing sufficiently with the drier fluid 1. The horizontal velocities have the correct shape, but the magnitude of the fluid 2 velocities is not consistent with the LES, suggesting the need for a horizontal drag term, or alternative couplings, in future formulations of the model.

The vertical profiles of some higher-order properties are shown in Figure 7. Of particular importance is the representation of subfilter turbulent kinetic energy, which is calculated as a prognostic variable in Equation (7) and is coupled to the subfilter velocity variances, turbulent length-scales, and turbulent mixing processes. The 2FSCM successfully predicts the fluid 2 subfilter TKE in

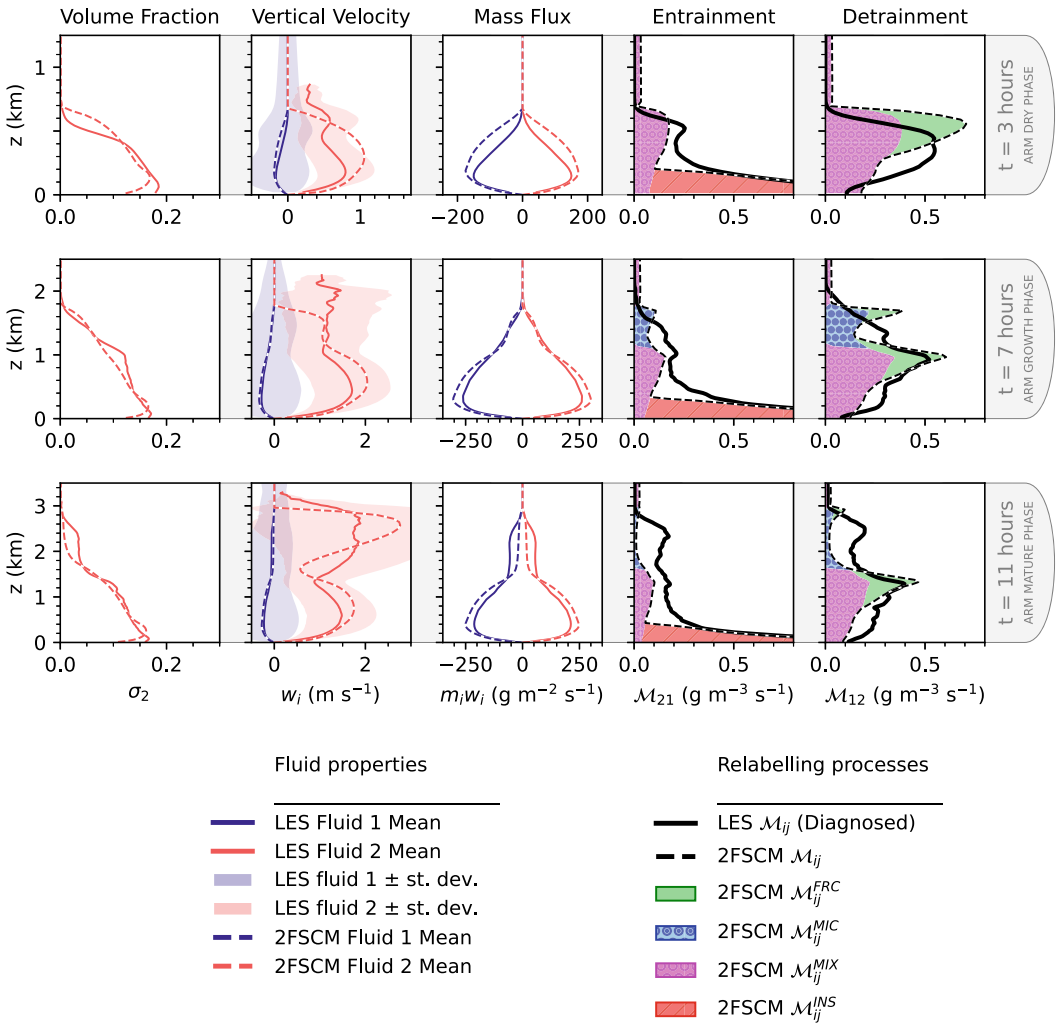

FIGURE 5 Vertical profiles for the volume fraction, vertical velocity, mass flux, entrainment, and detrainment for the ARM case. The profiles are given during spin-up of the moist convective boundary layer (top), growth of the cloud layer (middle), and the quasisteady state of the cloud layer (bottom). Conditionally averaged profiles diagnosed from the LES are given by the solid lines, and the 2FSCM profiles are given by the dashed lines. The lightly shaded regions show the one-standard-deviation range of the LES profiles. For the relabelling processes, the shaded styling corresponds to the processes described in Figure 3 [Colour figure can be viewed at wileyonlinelibrary.com]

the boundary layer and lower/mid cloud layer for the mid and later stages, however the fluid 2 profile is too large near the surface at the start of the simulation. The subfilter moisture variance for fluid 2 is too large in the lower cloud layer, which is responsible for the underrepresentation of liquid water and cloud fraction in this region of the domain (see Figure 5c). The dominant contribution to the excess moisture variance is the entrainment at cloud base, suggesting that too much dry air is being entrained. Also shown are the total contributions to the resolved potential temperature and moisture fluxes (black). The resolved flux contributions (diagnosed from the mean fluid properties) are generally well captured by the 2FSCM, although too much moisture is being transported out of the boundary layer, as noted in Figure 5. The grey lines show the total flux including subfilter contributions. As already noted in Efstathiou *et al.* (2020), the chosen fluid partitions (Equation 12) ensure that the majority of the fluxes are resolved, meaning there is less reliance on the subfilter contributions.

The results presented thus far demonstrate that the two-fluid model is able to capture the initiation, termination, and length-scales associated with shallow convection, and is generally able to capture the expected behaviour of the dynamics and thermodynamics. However, some biases have been noted, including a dry boundary layer, an undilute cloud layer, and low fluid 2 volume fraction in the cloud layer. These biases could be, in part, due to tuning to optimize other metrics. For example, Figure 8 shows the vertical profiles for an alternative

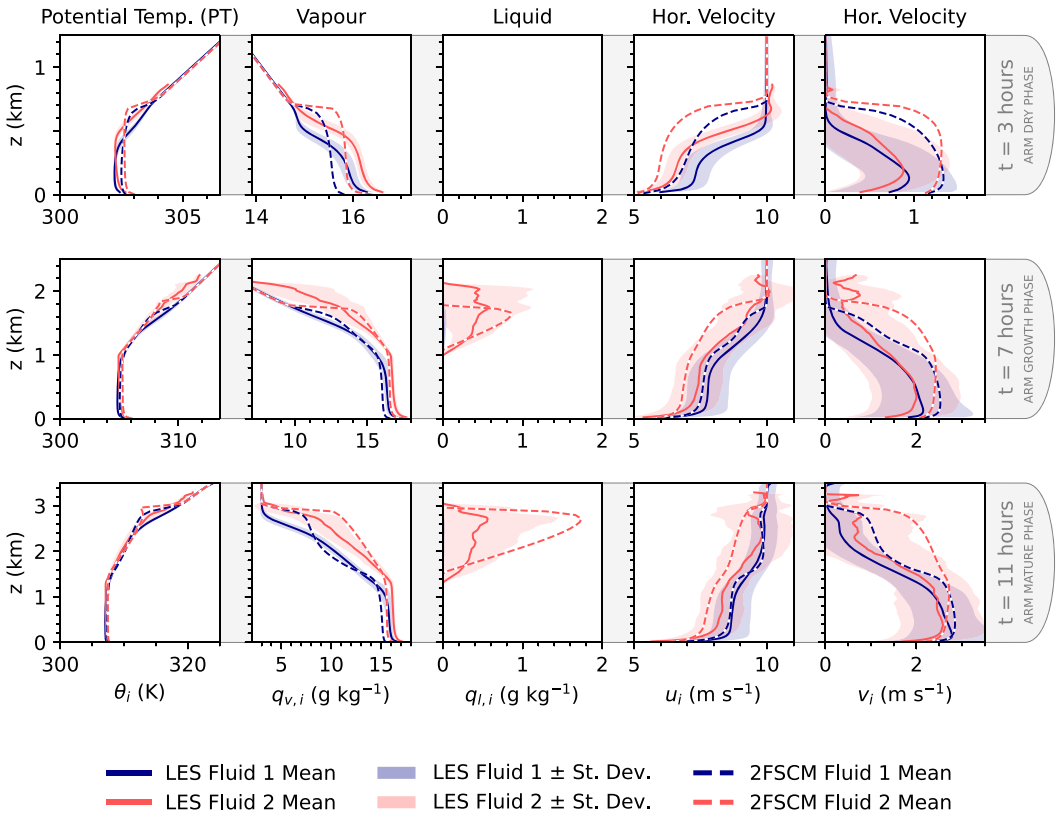

FIGURE 6 Vertical profiles of the potantial temperature, water vapour, liquid water, and the two components of horizontal velocity for the ARM case. The profiles are given during spin-up of the moist convective boundary layer (top), growth of the cloud layer (middle), and the quasisteady state of the cloud layer (bottom). Conditionally averaged profiles diagnosed from the LES are given by the solid lines, and the 2FSCM profiles are given by the dashed lines [Colour figure can be viewed at wileyonlinelibrary.com]

model configuration, in which the boundary layer is more moist and the fluid 2 cloud layer is more dilute and has more mass. However, results such as these are thought to be a case of getting the correct answer for the wrong reason, due to the significant underestimation of the fluid 2 TKE at all heights, resulting in unintended distributions of covariances, eddy diffusivity, entrainment, and detrainment. Such results hint at the potential of the 2FSCM, whilst also suggesting that modifications to the closures must be made to reach its full potential.

4.4 | Sensitivity to tunable parameters

In Section 4.2, various tunable parameters were described, which are designed to control the rate of relabelling of the fluids, the entrained/detrained fluid properties, the subfilter fluxes, and the dissipation rates. Documenting the sensitivity is an essential prerequisite to tuning. Testing how the cloud properties change with each parameter can also teach us about the importance of various processes. Figure 9 shows how the mean cloud fraction, mean cloud-base height, and mean cloud-top height change when the tunable parameters are adjusted by magnitudes up to ± 15%.

Of all the $b^{\mathrm{PROC}}_{\psi,ij}$ coefficients that control the properties entrained and detrained from the convective plumes, the cloud properties are most sensitive to the moisture coefficients in the cloud layer, as well as $b^{\mathrm{MIC}}_{\eta,12}$ and $b^{\mathrm{INS}}_{\eta,21}$.

- Decreasing $b^{\mathrm{MIC}}_{q,21}$ (resulting in higher entrained cloud-layer moisture) results in a higher cloud fraction due to the higher levels of saturated moisture in fluid 2. In Section 4.3, it was noted that the cloud fraction in the 2FSCM was too low, and Figure 4 suggests a lower value of $b^{\mathrm{MIC}}_{q,21}$ is consistent with the LES diagnostics. However, a lower $b^{\mathrm{MIC}}_{q,21}$ leads to an unsustainable moisture flux out of the boundary layer in the 2FSCM, which subsequently causes the cloud ensemble to collapse later in the simulation (similar to the collapses observed in the high-order closure scheme of Bogenschutz and Krueger, 2013).
- The fluid 2 liquid water profile is even more sensitive to $b^{\mathrm{MIC}}_{q,12}$, which controls the detrained liquid water in the

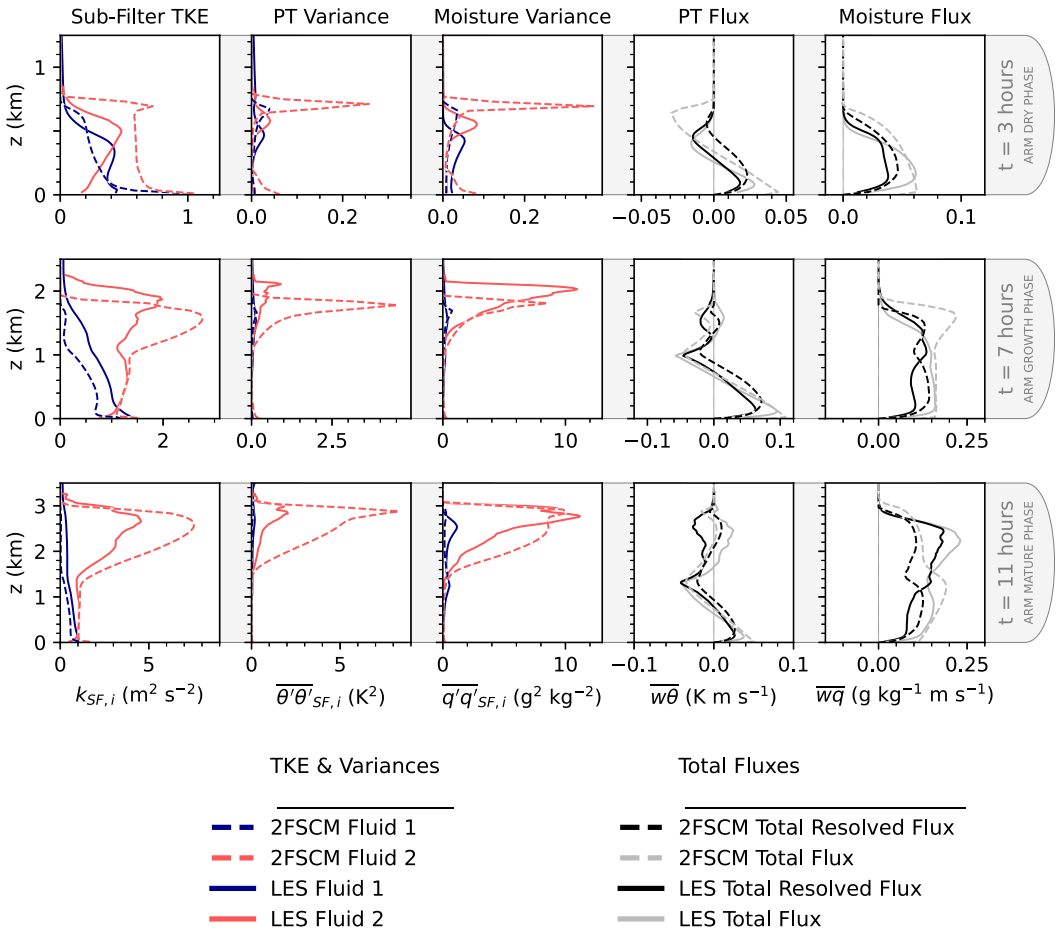

FIGURE 7 Vertical profiles for the subfilter TKE, the subfilter potential temperature variance, the subfilter moisture variance, the total buoyancy flux, and the total moisture flux for the ARM case. Each profile is presented during spin-up of the moist convective boundary layer (top), growth of the cloud layer (middle), and the quasisteady state of the cloud layer (bottom). Conditionally averaged profiles from the LES are given by the solid lines, and the 2FSCM profiles are given by the dashed lines [Colour figure can be viewed at wileyonlinelibrary.com]

cloud layer. Using a 10% lower coefficient can result in a cloud-top (defined as the 0.1% contour) that is several hundred metres higher. This is because the fluid 2 volume fraction in the 2FSCM is underrepresented in the upper cloud layer, meaning a smaller b coefficient will result in a significant increase to the remaining fluid 2 mean moisture in order to conserve the total moisture. This sensitivity could be avoided in future studies by adjusting the balance of the entrainment and detrainment terms to give the correct upper-cloud layer volume fraction. $b^{\mathrm{FRC}}_{q,12}$ has a similar but less extreme effect because the forced detrainment term acts only on the top fraction of the cloud layer. The cloud properties in the 2FSCM are also sensitive to the detrained entropy in the cloud layer, $b^{\mathrm{MIC}}_{\eta,12}$, which is also due to the underrepresented fluid 2 volume fraction.

- $b^{\mathrm{INS}}_{\eta,21}$ controls the buoyancy of fluid 2 at the surface, yet has a huge impact on the cloud properties—a demonstration of the tight coupling between the boundary layer and the cloud layer. An increase in this coefficient decreases the fluid 2 buoyancy, and therefore the boundary layer fluid 2 vertical velocity and the subfilter TKE. Subsequently, the boundary-layer detrainment terms $\mathcal{M}^{\mathrm{FRC}}_{12}$ and $\mathcal{M}^{\mathrm{MIC}}_{12}$ are smaller in magnitude, resulting in a higher cloud-base volume fraction and cloud fraction. $b^{\mathrm{INS}}_{\eta,21} = 1$ is used because the correct fluid 2 surface buoyancy is produced—using the LES-diagnosed value of $b^{\mathrm{INS}}_{\eta,21} \approx 0.5$ (Figure 4) results in double the magnitude of the diagnosed buoyancy and unrealistically high vertical velocities at all heights. It should be noted that a smaller coefficient for both $b^{\mathrm{INS}}_{\eta,21}$ and $b^{\mathrm{INS}}_{q,21}$ should be feasible with a different partitioning of the surface fluxes between fluid 1 and 2 (see Thuburn *et al.*, 2022b). This will be investigated further in future studies.

All of the $\mathcal{F}^{\mathrm{PROC}}$ coefficients affect cloud fraction significantly because they control the fluid 2 volume fraction in the cloud layer directly or indirectly. The height of the

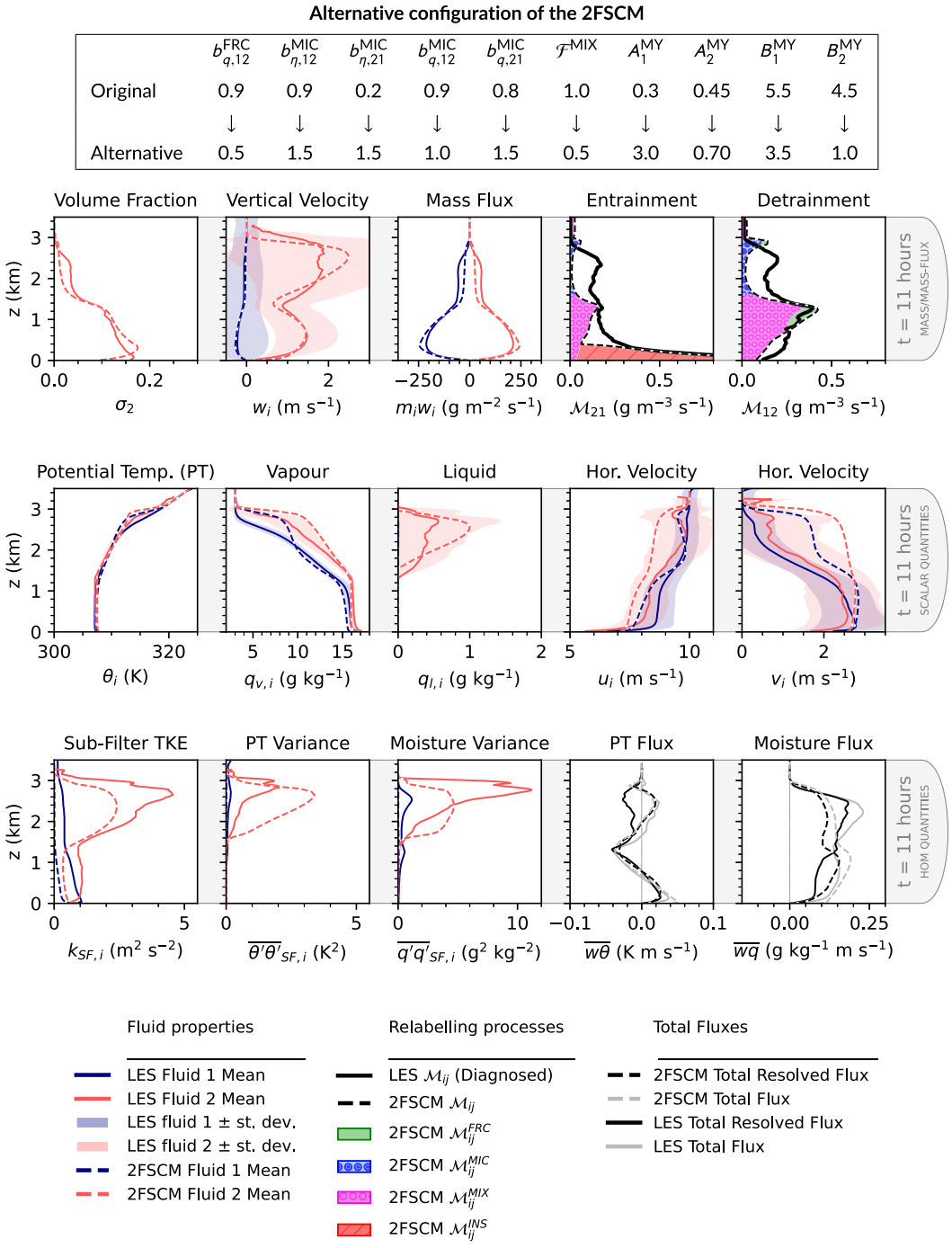

FIGURE 8 Vertical profiles of the mass-flux-related fields (top), scalar fluid properties (middle), and higher-order moment quantities (bottom) for the ARM case during the mature phase (11 hr), using an alternative model configuration. Conditionally averaged profiles from the LES are given by the solid lines, and the 2FSCM profiles are given by the dashed lines [Colour figure can be viewed at wileyonlinelibrary.com]

cloud base and cloud top are also sensitive to $\mathcal{F}^{\mathrm{MIX}}$ because the turbulent mixing term is active throughout the cloud layer.

The 2FSCM ARM results are not significantly sensitive to A_1^{MY}, the Mellor–Yamada coefficient that controls the subfilter flux of the horizontal and vertical velocity components. This is expected given that the subfilter flux is not a large term in the vertical velocity budget (although it is crucial for the stability of the two-fluid equations; Thuburn *et al.*, 2019). The 2FSCM is more sensitive to the other Mellor–Yamada coefficients such as A_2^{MY}, which controls the subfilter fluxes of the other scalar quantities. A decrease in the subfilter moisture flux (due to a smaller A_2^{MY}) is responsible for a reduction in the cloud fraction.

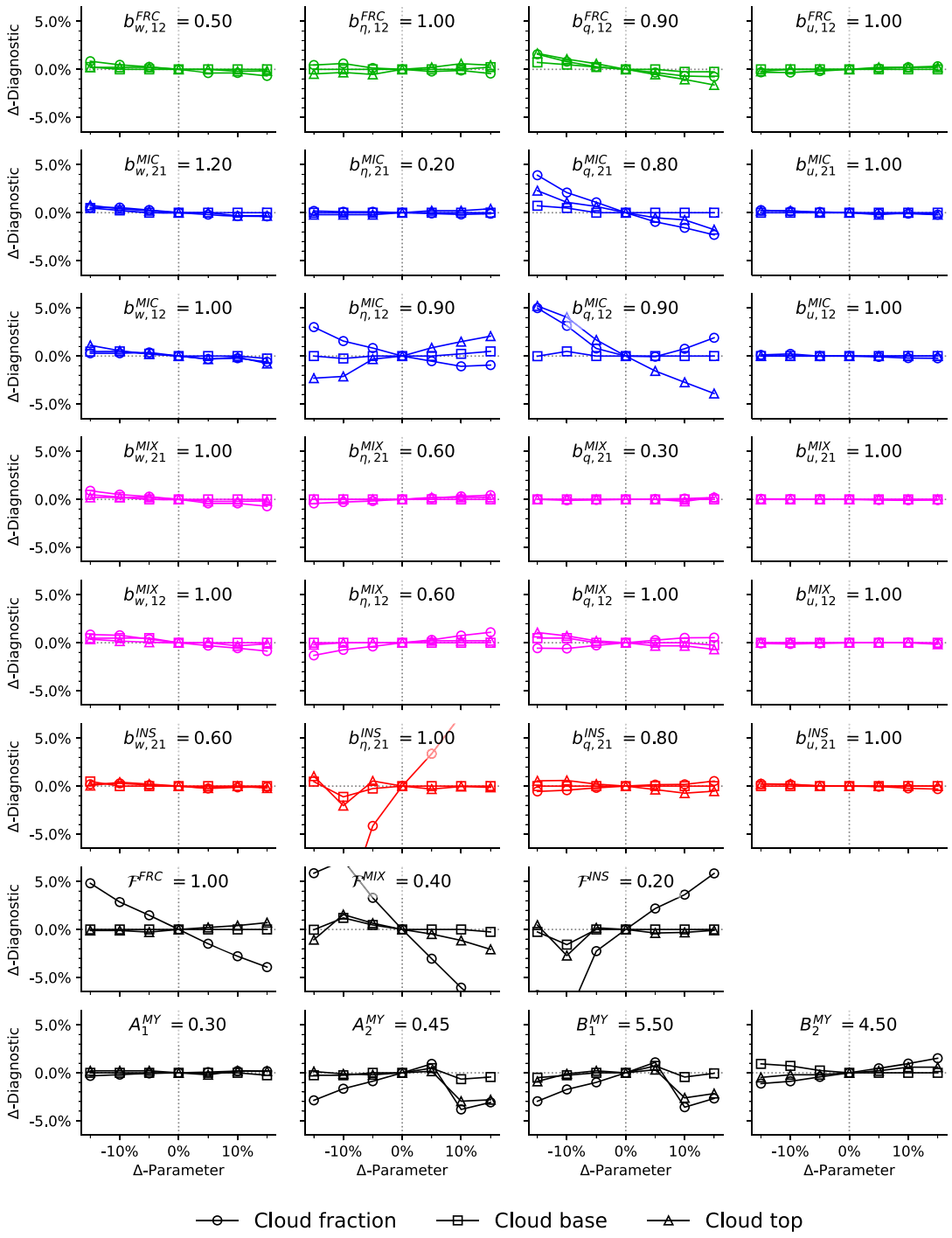

FIGURE 9 The sensitivity of the 2FSCM to the tunable parameters from entrainment/detrainment processes $\left(b_{\psi,ij}^{\mathrm{PROC}} \text{ and } \mathcal{F}^{\mathrm{PROC}}\right)$ and the subfilter-scale closures $\left(A_i^{\mathrm{MY}} \text{ and } B_i^{\mathrm{MY}}\right)$. The sensitivities for the mean cloud fraction (circles), mean cloud-base height (squares), and mean cloud-top height (triangles) are shown. Each parameter has been perturbed by up to ±15% from the base values displayed in each subplot heading [Colour figure can be viewed at wileyonlinelibrary.com]

It should be noted that the sensitivities for the TKE dissipation time-scale (B_1^{MY}) are similar to those of A_2^{MY} in all scenarios. This is because the eddy diffusivity is proportional to the TKE as well as A_2^{MY}. Given that B_1^{MY} controls the dissipation of the TKE, it proportionately affects the diffusivity of the scalar quantities relative to A_2^{MY}. It is also important to note that the nonlinear nature of this sensitivity is not surprising, because the TKE is tightly coupled

to various properties and processes, including covariances, diffusivity, entrainment, and detrainment.

5 | VERIFICATION WITH THE BOMEX CASE

Although the 2FSCM has been trialled successfully on the ARM case, an additional case study should be tested that has not been used to tune the model. The BOMEX case (Holland and Rasmusson, 1973; Nitta and Esbensen, 1974) presents different challenges compared with the ARM case, including the following.

- The BOMEX case study is located over sea instead of land, resulting in higher surface latent heat flux relative to the surface sensible heat flux. This will test whether the tuning of the model is applicable for a wide range of conditions.
- The surface fluxes are constant, rather than diurnally varying. This will test whether the model is able to maintain a steady state.
- The BOMEX case has various large-scale forcings that help maintain a quasisteady state. These terms (which are negligible in the ARM case) include large-scale subsidence, large-scale horizontal advection (which removes moisture from the domain), and radiative cooling. The magnitudes of these forcing terms are discussed in detail in Siebesma and Cuijpers (1995) and Siebesma *et al.* (2003), and all of the relevant terms have been included in the LES and 2FSCM simulations.

The MONC LES model used for the ARM case is also used for the BOMEX case. The horizontal domain is changed to $12.8 \times 12.8\,\mathrm{km}^2$ and the simulation is run for 6 hr.

Figure 2b shows the cloud evolution for both the LES and 2FSCM simulations. The LES profile shows a spin-up phase for the first hour of the simulation, after which a steady state is reached. Temporary peaks in the LES cloud fraction are due to individual clouds skewing the profile. The cloud base and cloud top are maintained at approximately 0.5 and 2.0 km respectively, at the 0.1% level. The 2FSCM has a 20% faster spin-up time and maintains a similar cloud base and cloud top. There is a marginal increase in the cloud base by 50 m over the course of the six-hour simulation, similar to the ARM case. As discussed in Section 4.3, this is due to the boundary layer drying too quickly. The peak cloud fraction at cloud base is 10% lower after 6 hr relative to the LES.

The vertical profiles for the BOMEX case after 6 hr are shown in Figure 10—these profiles change little between hours 5 and 6 in the 2FSCM. As with the ARM case, the boundary-layer volume fraction is modelled accurately in the 2FSCM, but the detrainment is slightly too strong in the upper cloud layer, with insufficient entrainment to compensate. Many of the cloud-layer properties are too large, including w_2, $q_{l,2}$, $k_{\mathrm{SF},2}$, and the fluid 2 variances, partially due to the lower fluid 2 volume fraction above 1 km. Despite this, the mass-weighted fluid 2 properties are being predicted correctly, including the mass flux, mass-weighted liquid water, and the resolved fluxes.

These results demonstrate that the 2FSCM is able to capture the physical processes of the moist convective boundary layer for a variety of different cases. Initiation and termination of shallow cumulus clouds are also modelled accurately. Nevertheless, it is clear that some of the biases observed in the ARM case are also present for the BOMEX case.

6 | CONCLUSION

This study closes the entrainment and detrainment formulations of the two-fluid single-column model from Thuburn *et al.,* (2022a; 2022b) by using LES data to diagnose the expected properties of entrained and detrained air. Other coefficients, such as the Mellor–Yamada parameters and the mixing rates, were guided using a gradient-descent algorithm that minimized the root-mean-square error of the cloud fraction and other mean profiles of the convective fluid. All coefficients were tuned for the diurnally varying ARM shallow cumulus case. The same model configuration was later used for the steady-state BOMEX case.

The two-fluid model was able to model accurately the initiation, evolution, and termination (where applicable) of shallow cumulus clouds for both case studies. Using the entrainment and detrainment coefficients displayed in Figure 9, the 2FSCM was able to reproduce the mean and turbulent profiles that were diagnosed from the LES data, particularly in the boundary layer and lower-cloud layer. The sensitivity study highlights the tight coupling and complexity of some of the feedbacks that operate in the 2FSCM. The results also provide valuable information that will help to improve the model formulation in future.

Results from the ARM and BOMEX simulations have also helped to identify some limitations of the current formulation of the 2FSCM.

- The model has a bias that causes excessive warming, drying, and deepening of the boundary layer (a phenomenon noted in other single-column model studies such as Neggers *et al.,* 2004; Lenderink *et al.,* 2004), because of excessive vertical mixing at the top of the

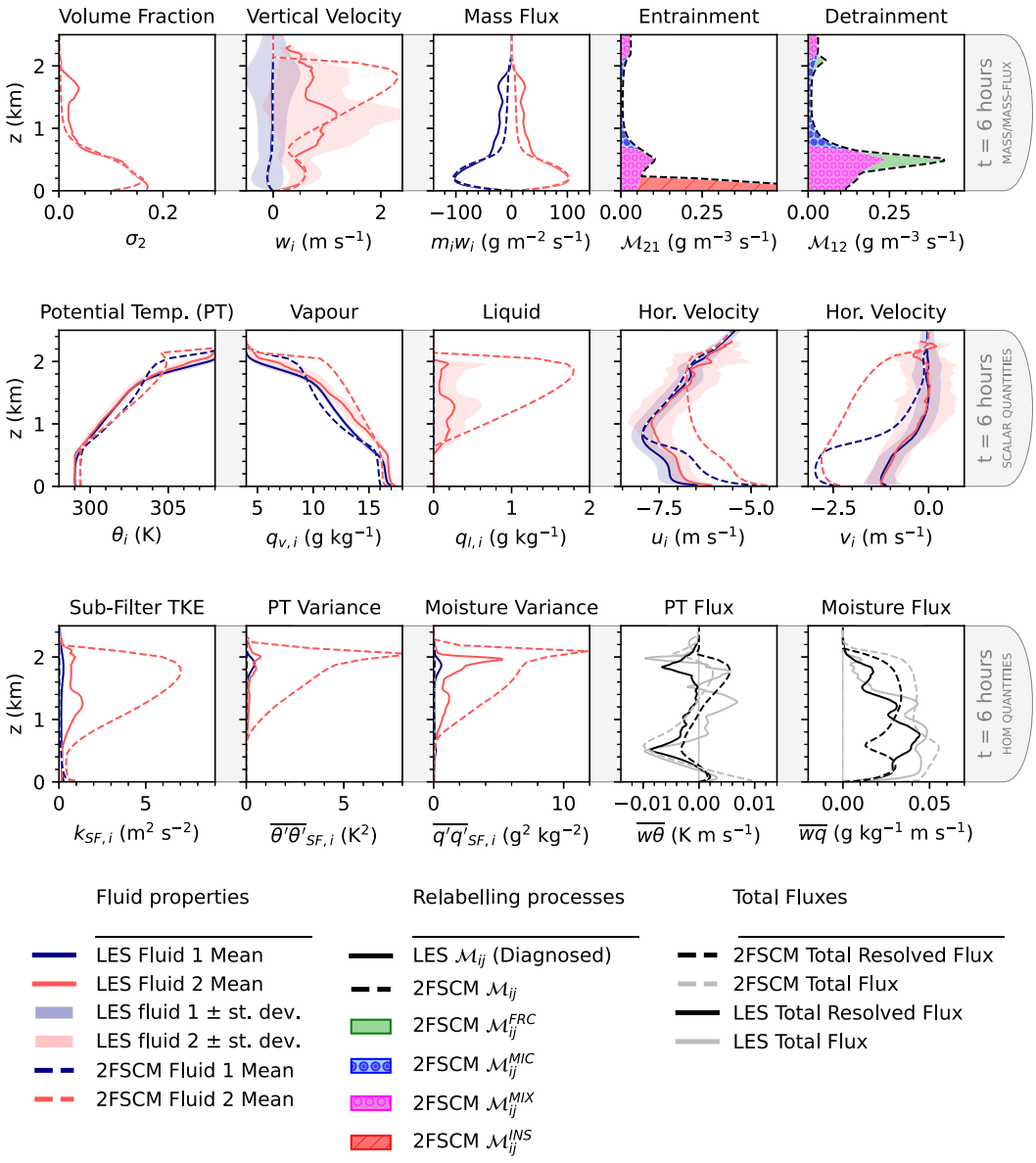

FIGURE 10 Vertical profiles of the mass-flux-related fields (top), scalar fluid properties (middle), and higher-order moment quantities (bottom) for the BOMEX case in a quasisteady state. Conditionally averaged profiles from the LES are given by the solid lines, and the 2FSCM profiles are given by the dashed lines [Colour figure can be viewed at wileyonlinelibrary.com]

boundary layer. As such, the cloud fraction is too low, the height of the cloud base increases too quickly, and the convective clouds terminate slightly too soon. In future studies, additional terms in the higher-order moment equations will be investigated that represent the fallback of overshooting thermals into the boundary layer, which may help reduce the loss of boundary-layer moisture.

- The quantity of liquid water in the fluid 2 cloud layer is not dilute enough, which could cause inaccuracies in microphysics schemes that are tightly coupled to the level of saturation. Various diagnostics suggest that there is insufficient entrainment in the cloud layer, resulting in an updraft that is too buoyant and excessively moist.
- This article has placed a significant emphasis on the budgets of the thermodynamic quantities. There is also a need to investigate and improve the momentum budgets (with a particular focus on the horizontal velocities). Obvious next steps would be to include horizontal drag terms, analogous to the vertical drag terms $\mathcal{P}_i$ used here, or to introduce pressure differences between fluids, such as those used in (Weller *et al.*, 2020; Shipley *et al.*, 2022).

- The current model formulation does not currently take into account the varying properties of multiple plumes that are present at the same time. There are at least two ways such differences could be taken into account. One is through more sophisticated entrainment and detrainment schemes that use suitable assumed distributions of subplume and interplume properties (such as Neggers, 2015). Another is through the inclusion of multiple plume types as additional fluids.

This study has demonstrated that shallow convection can be modelled if the relabelled fluid properties are represented accurately; here we have used LES diagnostics to constrain a simple "interpolation" model for these terms. However, future studies will focus on a unified and more physically based entrainment/detrainment scheme that uses probability density functions and higher-order terms to predict the relabelled fluid properties when entrainment or detrainment occurs.

Realizing the potential of the two-fluid approach will require its application in two- and three-dimensional models. The single-column model documented here is a necessary step towards the development of such a model.

AUTHOR CONTRIBUTIONS

William A. McIntyre: conceptualization; data curation; formal analysis; investigation; methodology; project administration; software; validation; visualization; writing – original draft. **Georgios A. Efstathiou:** conceptualization; data curation; formal analysis; methodology; project administration; software; writing – review and editing. **John Thuburn:** conceptualization; funding acquisition; methodology; project administration; software; validation; writing – review and editing.

ACKNOWLEDGEMENTS

This work was funded by the Natural Environment Research Council under Grants NE/N013123/1 and NE/T003863/1 as part of the ParaCon programme, as well as by the Weather and Climate Science for Service Partnership Southeast Asia under Grant SEA21_2.10.

We acknowledge use of the Monsoon2 system, a collaborative facility supplied under the Joint Weather and Climate Research Programme, a strategic partnership between the Met Office and the Natural Environment Research Council.

The particle trajectory simulation code was provided by Peter Clark (github.com/ReadingClouds/Trajectories). Simulations with the two-fluid single-column model were conducted using MultiFluidSCM (github.com/MultiFluidSCM).

We are grateful to Dr Yair Cohen and an anonymous reviewer for their constructive comments. We also thank Dr Hilary Weller and Dr Daniel Shipley for their valuable feedback.

ORCID

William A. McIntyre https://orcid.org/0000-0002-2715-9842
Georgios A. Efstathiou https://orcid.org/0000-0003-3469-8729
John Thuburn https://orcid.org/0000-0002-4598-546X

REFERENCES

Arakawa, A. (2004) The cumulus parameterization problem: past, present, and future. *Journal of Climate*, 17, 2493–2525.

Augstein, E., Riehl, H., Ostapoff, F. and Wagner, V. (1973) Mass and energy transports in an undisturbed Atlantic trade-wind flow. *Monthly Weather Review*, 101, 101–111.

Betts, A.K. (1986) A new convective adjustment scheme. Part I: observational and theoretical basis. *Quarterly Journal of the Royal Meteorological Society*, 112, 677–691.

Bogenschutz, P.A. and Krueger, S.K. (2013) A simplified PDF parameterization of subgrid-scale clouds and turbulence for cloud-resolving models. *Journal of Advances in Modeling Earth Systems*, 5, 195–211.

Brown, A., Cederwall, R., Chlond, A., Duynkerke, P., Golaz, J.-C., Khairoutdinov, M., Lewellen, D., Lock, A., MacVean, M., Moeng, C.-H., Neggers, R., Siebesma, A.P. and Stevens, B. (2002) Large-eddy simulation of the diurnal cycle of shallow cumulus convection over land. *Quarterly Journal of the Royal Meteorological Society*, 128, 1075–1093.

Clark, P., Denby, L., Efstathiou, G.A. and Webb, T.L. (2022) Mixed offline/online trajectories and object-tracking for process research. *Journal of Advances in Modeling Earth Systems*. (submitted).

Cohen, Y., Lopez-Gomez, I., Jaruga, A., He, J., Kaul, C.M. and Schneider, T. (2020) Unified entrainment and detrainment closures for extended eddy-diffusivity mass-flux schemes. *Journal of Advances in Modeling Earth Systems*, 12, e2020MS002162.

Couvreux, F., Hourdin, F. and Rio, C. (2010) Resolved versus parametrized boundary-layer plumes. Part I: a parametrization-oriented conditional sampling in large-eddy simulations. *Boundary-Layer Meteorology*, 134, 441–458.

Dawe, J.T. and Austin, P.H. (2011) The influence of the cloud shell on tracer budget measurements of LES cloud entrainment. *Journal of the Atmospheric Sciences*, 68, 2909–2920.

De Rooy, W.C., Bechtold, P., Fröhlich, K., Hohenegger, C., Jonker, H., Mironov, D., Siebesma, A.P., Teixeira, J. and Yano, J.-I. (2013) Entrainment and detrainment in cumulus convection: an overview. *Quarterly Journal of the Royal Meteorological Society*, 139, 1–19.

Derbyshire, S., Maidens, A., Milton, S., Stratton, R. and Willett, M. (2011) Adaptive detrainment in a convective parametrization. *Quarterly Journal of the Royal Meteorological Society*, 137, 1856–1871.

Efstathiou, G.A., Thuburn, J. and Beare, R.J. (2020) Diagnosing coherent structures in the convective boundary

layer by optimizing their vertical turbulent scalar transfer. *Boundary-Layer Meteorology*, 174, 119–144.

Fletcher, J.K. and Bretherton, C.S. (2010) Evaluating boundary layer-based mass flux closures using cloud-resolving model simulations of deep convection. *Journal of the Atmospheric Sciences*, 67, 2212–2225.

Gheusi, F. and Stein, J. (2002) Lagrangian description of airflows using Eulerian passive tracers. *Quarterly Journal of the Royal Meteorological Society*, 128, 337–360.

Golaz, J.-C., Larson, V.E. and Cotton, W.R. (2002) A PDF-based model for boundary layer clouds. Part II: model results. *Journal of Atmospheric Sciences*, 59, 3552–3571.

Gregory, D. and Rowntree, P. (1990) A mass flux convection scheme with representation of cloud ensemble characteristics and stability-dependent closure. *Monthly Weather Review*, 118, 1483–1506.

Gross, M., Wan, H., Rasch, P.J., Caldwell, P.M., Williamson, D.L., Klocke, D., Jablonowski, C., Thatcher, D.R., Wood, N., Cullen, M., Beare, B., Willett, M., Lemarié, F., Blayo, E., Malardel, S., Termonia, P., Gassmann, A., Lauritzen, P.H., Johansen, H., Zarzycki, C.M., Sakaguchi, K. and Leung, R. (2018) Physics–dynamics coupling in weather, climate, and earth system models: challenges and recent progress. *Monthly Weather Review*, 146, 3505–3544.

He, J., Cohen, Y., Lopez-Gomez, I., Jaruga, A. and Schneider, T. (2020) An improved perturbation pressure closure for eddy-diffusivity mass-flux schemes. *Earth and Space Science Open Archive*. https://doi.org/10.1002/essoar.10505084.2.

Holland, J.Z. and Rasmusson, E.M. (1973) Measurements of the atmospheric mass, energy, and momentum budgets over a 500-kilometer square of tropical ocean. *Monthly Weather Review*, 101, 44–55.

Holloway, C.E., Petch, J.C., Beare, R.J., Bechtold, P., Craig, G.C., Derbyshire, S.H., Donner, L.J., Field, P.R., Gray, S.L., Marsham, J.H., Parker, D.J., Plant, R.S., Roberts, N.M., Schultz, D.M., Stirling, A.J. and Woolnough, S.J. (2014) Understanding and representing atmospheric convection across scales: recommendations from the meeting held at Dartington hall, Devon, UK, 28–30 January 2013. *Atmospheric Science Letters*, 15, 348–353.

Houghton, H.G. and Cramer, H.E. (1951) A theory of entrainment in convective currents. *Journal of Meteorology*, 8, 95–102.

Kain, J.S. and Fritsch, J.M. (1990) A one-dimensional entraining/detraining plume model and its application in convective parameterization. *Journal of the Atmospheric Sciences*, 47, 2784–2802.

Kuell, V. and Bott, A. (2008) A hybrid convection scheme for use in non-hydrostatic numerical weather prediction models. *Meteorologische Zeitschrift*, 17, 775–783.

Kwon, Y.C. and Hong, S.-Y. (2017) A mass-flux cumulus parameterization scheme across gray-zone resolutions. *Monthly Weather Review*, 145, 583–598.

Lenderink, G., Siebesma, A.P., Cheinet, S., Irons, S., Jones, C.G., Marquet, P., Müller, F., Olmeda, D., Calvo, J., Sanchez, E. and Soares, P.M.M. (2004) The diurnal cycle of shallow cumulus clouds over land: a single-column model intercomparison study. *Quarterly Journal of the Royal Meteorological Society*, 130, 3339–3364.

Lopez-Gomez, I., Cohen, Y., He, J., Jaruga, A. and Schneider, T. (2020) A generalized mixing length closure for eddy-diffusivity mass-flux schemes of turbulence and convection. *Journal of Advances in Modeling Earth Systems*, 12, e2020MS002161.

McIntyre, W. (2020) *Multi-fluid modelling of dry convection*. Ph.D. thesis, University of Reading.

Mellor, G.L. and Yamada, T. (1982) Development of a turbulence closure model for geophysical fluid problem. *Reviews of Geophysics and Space Physics*, 20, 851–875.

Neggers, R. (2015) Exploring bin-macrophysics models for moist convective transport and clouds. *Journal of Advances in Modeling Earth Systems*, 7, 2079–2104.

Neggers, R., Siebesma, A. and Jonker, H. (2002) A multiparcel model for shallow cumulus convection. *Journal of the Atmospheric Sciences*, 59, 1655–1668.

Neggers, R., Siebesma, A., Lenderink, G. and Holtslag, A. (2004) An evaluation of mass flux closures for diurnal cycles of shallow cumulus. *Monthly Weather Review*, 132, 2525–2538.

Nitta, T. and Esbensen, S. (1974) Heat and moisture budget analyses using BOMEX data. *Monthly Weather Review*, 102, 17–28.

Pergaud, J., Masson, V., Malardel, S. and Couvreux, F. (2009) A parameterization of dry thermals and shallow cumuli for mesoscale numerical weather prediction. *Boundary-Layer Meteorology*, 132, 83–106.

Rio, C. and Hourdin, F. (2008) A thermal plume model for the convective boundary layer: representation of cumulus clouds. *Journal of the Atmospheric Sciences*, 65, 407–425.

Satoh, M., Stevens, B., Judt, F., Khairoutdinov, M., Lin, S.-J., Putman, W.M. and Düben, P. (2019) Global cloud-resolving models. *Current Climate Change Reports*, 5, 172–184.

Shipley, D. (2021) *Multi-fluid modelling of idealized convection*. Ph.D. thesis, University of Reading.

Shipley, D., Weller, H., Clark, P.A. and McIntyre, W.A. (2022) Two-fluid single-column modelling of Rayleigh–Bénard convection as a step towards multi-fluid modelling of atmospheric convection. *Quarterly Journal of the Royal Meteorological Society*, 148, 351–377.

Siebesma, A. and Cuijpers, J. (1995) Evaluation of parametric assumptions for shallow cumulus convection. *Journal of Atmospheric Sciences*, 52, 650–666.

Siebesma, A.P., Bretherton, C.S., Brown, A., Chlond, A., Cuxart, J., Duynkerke, P.G., Jiang, H., Khairoutdinov, M., Lewellen, D., Moeng, C.-H., Sanchez, E., Stevens, B. and Stevens, D.E. (2003) A large eddy simulation intercomparison study of shallow cumulus convection. *Journal of the Atmospheric Sciences*, 60, 1201–1219.

Smagorinsky, J. (1963) General circulation experiments with the primitive equations: I. The basic experiment. *Monthly Weather Review*, 91, 99–164.

Soares, P., Miranda, P., Siebesma, A. and Teixeira, J. (2004) An eddy-diffusivity/mass-flux parametrization for dry and shallow cumulus convection. *Quarterly Journal of the Royal Meteorological Society*, 130, 3365–3383.

Stirling, A. and Stratton, R. (2012) Entrainment processes in the diurnal cycle of deep convection over land. *Quarterly Journal of the Royal Meteorological Society*, 138, 1135–1149.

Tan, Z., Kaul, C.M., Pressel, K.G., Cohen, Y., Schneider, T. and Teixeira, J. (2018) An extended eddy-diffusivity mass-flux scheme for unified representation of subgrid-scale turbulence and convection. *Journal of Advances in Modeling Earth Systems*, 10, 770–800.

Thuburn, J., Efstathiou, G.A. and Beare, R.J. (2019) A two-fluid single-column model of the dry, shear-free, convective boundary layer. *Quarterly Journal of the Royal Meteorological Society.*, 145, 1535–1550.

Thuburn, J., Efstathiou, G.A. and McIntyre, W.A. (2022a) A two-fluid single-column model of turbulent shallow convection, part I: turbulence equations in the multi-fluid framework. *Quarterly*

Journal of the Royal Meteorological Society. https://doi.org/10.1002/qj.4366

Thuburn, J., Efstathiou, G.A. and McIntyre, W.A. (2022b) A two-fluid single-column model of turbulent shallow convection, part II: single-column model formulation and numerics. *Quarterly Journal of the Royal Meteorological Society*. https://doi.org/10.1002/qj.4366

Thuburn, J., Weller, H., Vallis, G.K., Beare, R.J. and Whitall, M. (2018) A framework for convection and boundary layer parameterization derived from conditional filtering. *Journal of the Atmospheric Sciences*, 75, 965–981.

Weller, H., McIntyre, W. and Shipley, D. (2020) Multifluids for representing subgrid-scale convection. *Journal of Advances in Modeling Earth Systems*, 12, e2019MS001966.

Weller, H. and McIntyre, W.A. (2019) Numerical solution of the conditionally averaged equations for representing net mass flux due to convection. *Quarterly Journal of the Royal Meteorological Society*, 145, 1337–1353.

Willett, M. and Whitall, M. (2017) *A simple prognostic based convective entrainment rate for the unified model: description and tests*. Met Office. Forecasting Research Tech. Rep. 617.

Yeo, K. and Romps, D.M. (2013) Measurement of convective entrainment using Lagrangian particles. *Journal of the Atmospheric Sciences*, 70, 266–277.

How to cite this article: McIntyre, W.A., Efstathiou, G.A. & Thuburn, J. (2022) A two-fluid single-column model of turbulent shallow convection. Part III: Results and parameter sensitivity. *Quarterly Journal of the Royal Meteorological Society*, 1–20. Available from: https://doi.org/10.1002/qj.4390